THE ASTROPHYSICAL JOURNAL, 590:225–237, 2003 June 10

# *XMM-NEWTON* OBSERVATIONS OF THE PERSEUS CLUSTER. I. THE TEMPERATURE AND SURFACE BRIGHTNESS STRUCTURE

E. CHURAZOV,[1,2] W. FORMAN,[3] C. JONES,[3] AND H. BÖHRINGER[4]

*Received 2002 November 8; accepted 2003 February 14*

## ABSTRACT

We present preliminary results of a *XMM-Newton* 50 ks observation of the Perseus Cluster that provides an unprecedented view of the central 0.5 Mpc region. The projected gas temperature declines smoothly by a factor of 2 from a maximum value of $\sim 7$ keV in the outer regions to just above 3 keV at the cluster center. Over this same range, the heavy-element abundance rises slowly from 0.4 to 0.5 solar as the radius decreases from $14'$ to $5'$, and then it rises to a peak of almost 0.7 solar at $1\overset{\prime}{.}25$ before declining to 0.4 at the center. The global east-west asymmetry of the gas temperature and surface brightness distributions, approximately aligned with the chain of bright galaxies, suggests an ongoing merger, although the modest degree of the observed asymmetry certainly excludes a major merger interpretation. The chain of galaxies probably traces the filament along which accretion started some time ago and is continuing at the present time. A cold and dense (low-entropy) cluster core like Perseus is probably well "protected" against the penetration of the gas of infalling groups and poor clusters, whereas in noncooling core clusters such as Coma and A1367, infalling subclusters can penetrate deeply into the core region. In Perseus, gas associated with infalling groups may be stripped completely at the outskirts of the main cluster and only compression waves (shocks) may reach the central regions. We argue, and show supporting simulations, that the passage of such a wave(s) can qualitatively explain the overall horseshoe shaped appearance of the gas temperature map (the hot horseshoe surrounds the colder, low-entropy core) as well as other features of the Perseus Cluster core. These simulations also show that as compression waves traverse the cluster core, they can induce oscillatory motion of the cluster gas that can generate multiple sharp "edges" on opposite sides of the central galaxy. Gas motions induced by mergers may be a natural way to explain the high frequency of "edges" seen in clusters with cooling cores.

*Subject headings:* cooling flows — galaxies: active — galaxies: clusters: individual (Perseus) — galaxies: individual (NGC 1275) — X-rays: galaxies — X-rays: galaxies: clusters

## 1. INTRODUCTION

The Perseus Cluster of galaxies (Abell 426) is the X-ray–brightest nearby cluster (with $z = 0.01756$, $1'$ corresponds to $\sim$30 kpc [29.7 kpc] for $H_0 = 50$ km s$^{-1}$ Mpc$^{-1}$, which we use throughout). It was first reported as an extended X-ray source from *Uhuru* observations (Forman et al. 1972), and the first images (Gorenstein et al. 1978; see also Fabian et al. 1974; Wolff et al. 1974; Malina et al. 1978) provided a glimpse of the X-ray structure of Perseus. Detailed X-ray images were obtained with the *Einstein* IPC (Branduardi-Raymont et al. 1981) and HRI (Fabian et al. 1981), with the *ROSAT* PSPC (Schwarz et al. 1992; Ettori, Fabian, & White 1998) and HRI (Böhringer et al. 1993), and recently with *Chandra* (Fabian et al. 2000; Schmidt, Fabian, & Sanders 2002). The cluster has a prominent X-ray surface brightness peak centered on the active galaxy NGC 1275, containing a strong core-dominated radio source (Per A, 3C 84) surrounded by a lower surface brightness halo (e.g., Pedlar et al. 1990; Sijbring 1993). Many studies have explored the correlations between X-ray, radio, optical, and ultraviolet emission in the core (see, e.g., McNamara, O'Connell, & Sarazin 1996 and references therein). The proximity and brightness of the cluster make it a natural target for studies of a relatively relaxed cluster with a cold core. In this paper we report preliminary results of the *XMM-Newton* 50 ks observations of the Perseus Cluster.

The structure of the paper is as follows: in § 2 we discuss *XMM-Newton* observations of the cluster, in § 3 we describe the analysis of the data and present the results, in § 4 we discuss possible implications of the results, and in § 5 we summarize our findings. The analysis of the substructure in the very core (less than $2'$) of the Perseus Cluster and details of the heavy-element abundance and distribution are beyond the scope of this paper and will be reported in subsequent publications.

## 2. OBSERVATIONS AND BACKGROUND SUBTRACTION

The core of the Perseus Cluster was observed with *XMM-Newton* on 2001 January 30 with a total integration time of $\sim$53 ks (observation 00851101). The pointing was centered on NGC 1275 (Fig. 1). We report below on the results obtained with the EPIC-MOS CCD array instrument only. Results from the Reflection Grating Spectrometer (RGS) and another CCD array, EPIC-pn, will be reported elsewhere. Calibrated event lists were generated using SAS version 5.3. As is known, the MOS background has a steady (quiescent) component partly associated with the cosmic X-ray background and a variable component due to

---

[1] Max-Planck-Institut für Astrophysik, Karl-Schwarzschild-Strasse 1, 85740 Garching, Germany.

[2] Space Research Institute (IKI), Profsoyuznaya 84/32, Moscow 117810, Russia.

[3] Harvard-Smithsonian Center for Astrophysics, 60 Garden Street, Cambridge, MA 02138.

[4] Max-Planck-Institut für Extraterrestrische Physik, P.O. Box 1603, 85740 Garching, Germany.

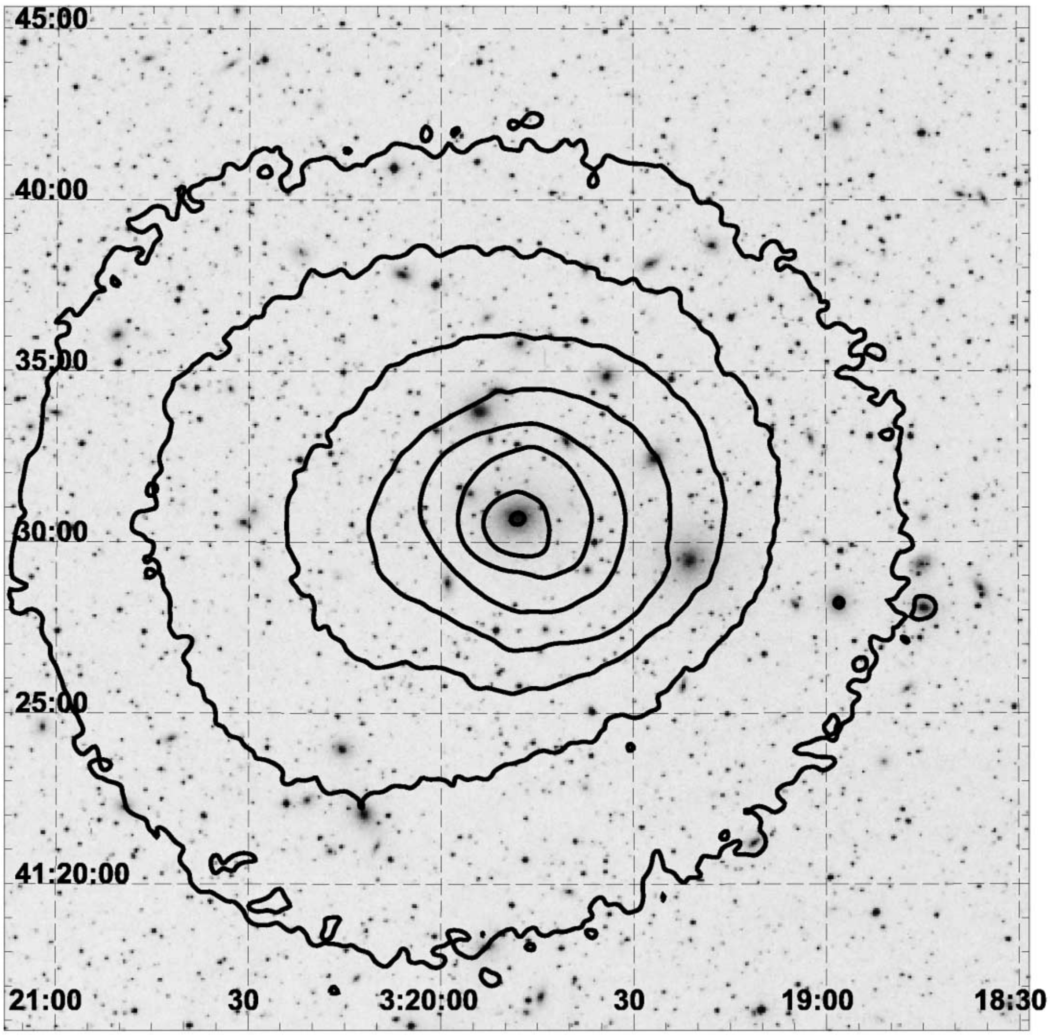

FIG. 1.—Surface brightness contours in the 0.3–5 keV energy range (corrected for the background and telescope vignetting) superposed onto a Digitized Sky Survey optical image ($30' \times 30'$). The X-ray image has been smoothed with an $8''$ Gaussian. The central galaxy is NGC 1275. A chain of bright galaxies is visible to the west.

charged particles (e.g., Lumb et al. 2002). To check the level of the variable background component, we used the same tracer as implemented in the SAS task *emchain*, i.e., the count rate of events with energy deposited in a single pixel higher than a threshold value ("*REJECTED_BY_GATTI*" in SAS notation). Although there are no obvious spikes in the light curve of such events, the count rate is several times higher than the recommended threshold value for the entire observation, indicating a significantly enhanced background level. Thus a straightforward application of the recommended cleaning procedure (using *emchain* default settings) would remove essentially all the data. To use the data set, we had to adopt special procedures to correct for the variable background component. As a first step, the steady component of the background was subtracted using data from blank field observations provided by the *XMM* SOC site (background data files are from 2002 January; see Lumb et al. 2002). The spectra of all but the central chip were accumulated for MOS1 and MOS2. Assuming that the variable component of the background has a power-law shape (in counts/channel space) with the slope of $B(E) = A \times E^{\alpha}$ and using the data in the 11–12 keV range, we calculated the normalization of the variable component. The slope $\alpha$ of the variable background spectrum is known to vary from observation to observation and (rather arbitrarily) has been fixed at $\alpha = -0.45$. We then assumed that the intensity of the variable component per unit area is constant across the detector and corrected all observed spectra for this variable component. The sample source and background spectra for the $8'$–$13'.75$ annulus are shown in Figure 2. The same procedure applied to the publicly available data sets with the "quiescent" background typically yields a normalization for the additional background component that is at least an order of magnitude lower.

To verify the quality of the background subtraction procedure, we used a publicly available 30 ks observation (observation ID 0100240801) performed $\sim$14 hr after the end of the Perseus observation. In this observation the background level was still enchanced compared to the quiescent level, although a factor of $\sim$2 lower than in the Perseus observation. There are no strong sources in this field (apart from the target, a compact source), and it is easier to see

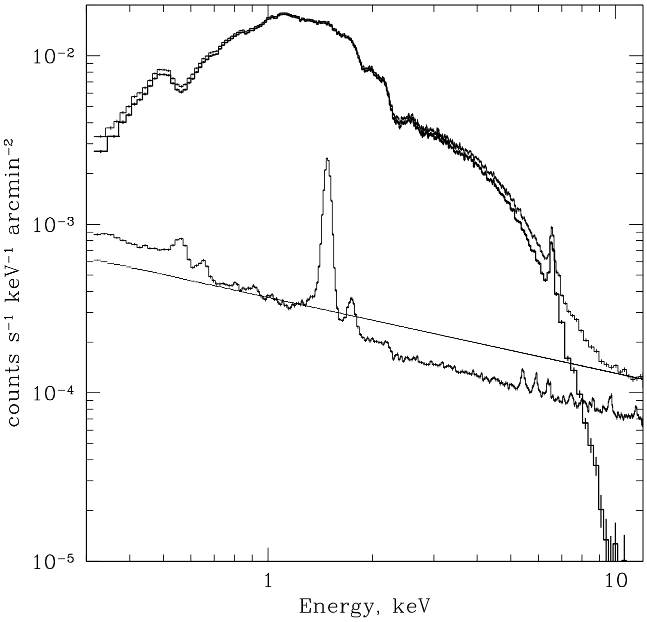

FIG. 2.—Spectrum of the $8'$–$13.75'$ annulus around NGC 1275 and the background spectrum. The two lower curves show the blank field "quiescent" background and the additional "flare" background component (power law) assumed in the analysis. Two upper curves show the source spectrum with the quiescent background subtracted (*upper curve*) and the source spectrum with both the quiescent and flare background components subtracted (*lower thick curve*). The normalization of the flare background has been estimated using the data above ∼11 keV.

how well the background is corrected in the regions far from the center of the field of view. For this data set we repeated exactly the same background correction procedure as for the Perseus observation. The results are shown in Figure 3. One can see that above ∼4 keV the predicted extra background component matches almost perfectly the accumulated spectrum (corrected for quiescent background). Below 2 keV some residuals are present, but given the brightness of Perseus at these energies (factor of 10–100 brighter than the background), such residuals have no significant impact on the results of the spectral fits.

The procedure and functions described above are the result of extensive tests with various shapes of the additional background and different methods to determine its normalization. The results reported below were found to be robust to the remaining uncertainties in the background subtraction. Further refinement of the background correction procedure may change slightly some of the numerical values, in particular the maximum gas temperature close to the edge of the field of view by ∼5%–10%, but cannot affect any of the principle results in the paper. More subtle features, like the limits on the possible nonthermal emission components, which are in principle attainable with the current observation are deferred to future work. For the same reason, we report only on the MOS observation, for which we achieved the most robust results.

For the subsequent analysis we used MOS data with patterns in the range 0–12 and the recommended value of the flag (XMM_EA). For the spectral analysis we use one of the MOS response matrixes provided by the *XMM* SOC (namely, "m1_thin1v9q19t5r5_all_15.rsp") and assume that the same response (corrected for energy-dependent vignetting) is applicable for all regions.

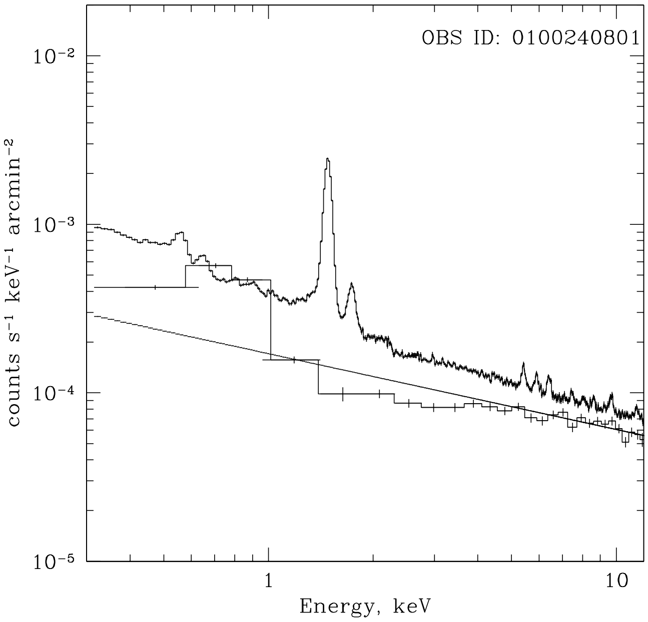

FIG. 3.—Same as in the previous figure, but for the observation performed ∼14 hr after the end of the Perseus observation. The background level was still enchanced compared to the quiescent state, although a factor of ∼2 lower than in the Perseus observation. The upper curve shows the quiescent background spectrum. The histogram is the spectrum accumulated over the $8'$–$13'.75$ annulus and corrected for the quiescent background. The power law shows the predicted "flare" background component, obtained with the same procedure as was used for the Perseus observation.

## 3. ANALYSIS

Although the cluster is not perfectly symmetric (see Fig. 1), it is illustrative to derive the radial dependence of major parameters, in particular the density, temperature, and heavy-element abundance, assuming spherical symmetry with the center at NGC 1275.

The radial dependence of the surface brightness is shown in Figure 4. The dotted line shows the expected profile (taking into account the point-spread function [PSF] of the telescope) for a point source plus constant surface brightness. The central excess (within $10''$) is therefore consistent with being due to the contribution of the unresolved, compact source—the nucleus of NGC 1275.

### 3.1. *Spectrum of NGC 1275*

Given the *XMM-Newton* spatial resolution and complicated surface brightness distribution near the cluster core, the precise determination of the NGC 1275 nuclear spectrum is difficult. We used the central $14''$ (radius) circle and the $14''$–$28''$ annulus as the source and background regions, respectively. The resulting spectrum is shown in Figure 5. It is fairly well fitted with an absorbed ($N_{\rm H} = 1.2 \times 10^{21}$ cm$^{-2}$) power law with a photon index of 1.65 and a narrow line at an energy of 6.289 keV (with a 1 $\sigma$ confidence interval from 6.276 to 6.313 keV) and an equivalent width of ∼165 eV. The assumption that the line is due to fluorescent emission of neutral iron at 6.4 keV implies a redshift of $z = 0.0176 \pm 0.003$, fully consistent with the optically determined redshift of NGC 1275 ($z = 0.01756$). A significant amount of cold gas and dust is known to be associated with the high-velocity (HV) system (Minkowski

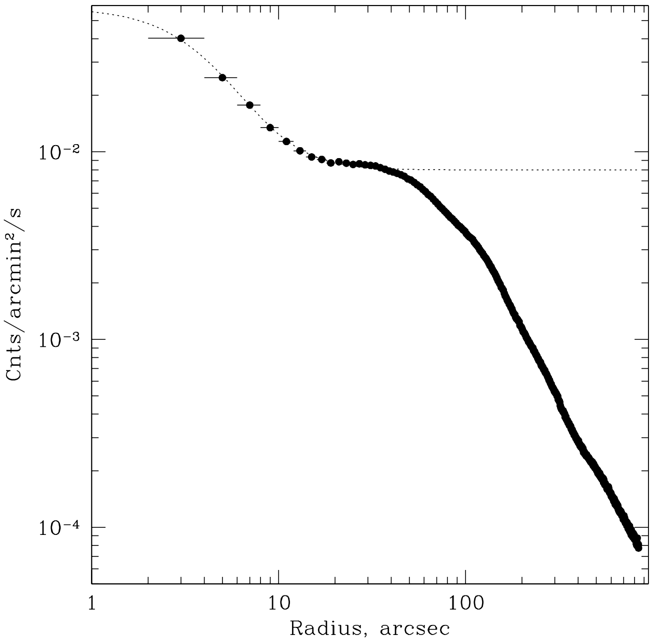

FIG. 4.—Radial dependence of the surface brightness in the 0.3–5 keV band. The dotted line shows the sum of the telescope PSF plus a constant, illustrating that the central excess is consistent with being due to the NGC 1275 nucleus contribution.

1957; see also Conselice, Gallagher, & Wyse 2001), but the excellent agreement between the redshifts of the line and the galaxy indicates that reprocessing by the HV gas does not contribute significantly to the observed spectrum. The 6.7 keV line, which is dominant in the cluster gas emission, is very weak in the nuclear spectrum, suggesting that the background has been subtracted with sufficient accuracy. We conclude that the observed spectrum of the nucleus is consistent with typical active galactic nucleus (AGN) spectra. The luminosity of the nucleus derived from the best-fit parameters is of the order of $10^{43}$ ergs $s^{-1}$ in the 0.5–8 keV range and is subject to systematic uncertainties (at the level of 20%) due to background subtraction and PSF correction.

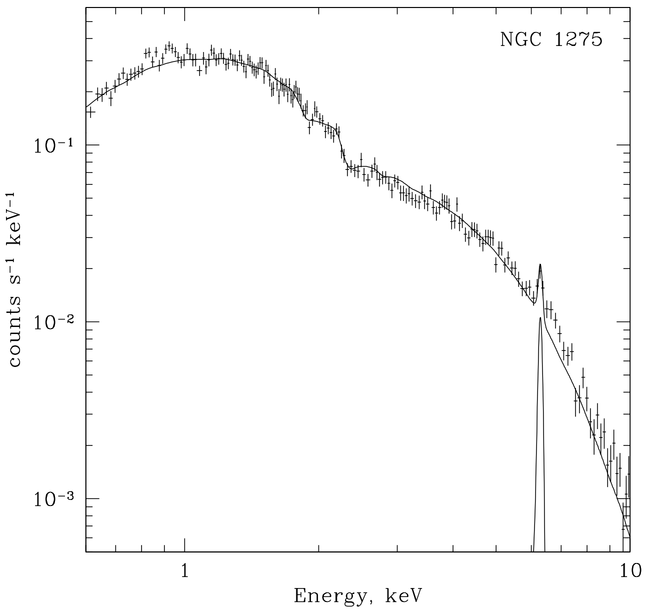

FIG. 5.—NGC 1275 spectrum determined as the difference between the spectra extracted from the 14″ (radius) circle and the annulus from 14″ to 28″. The position of the line is consistent with the neutral iron fluorescent line at 6.4 keV with redshift of 0.0176.

### 3.2. *Projected Parameters*

Spectra were accumulated in a set of annuli centered on NGC 1275. The resulting spectra were fitted (in the 0.5–9 keV range) with a single-temperature APEC (Smith et al. 2001) model in XSPEC (version 11.2.0; Arnaud 1996) with the gas temperature $T_e$, abundance of heavy elements $Z$ (relative to the solar values of Anders & Grevesse 1989), and low-energy photoelectric absorption column density $N_{\rm H}$ as free parameters. The redshift has been fixed at the optically determined value for NGC 1275: $z = 0.01756$ (Strauss et al. 1992). The projected radial dependence of all parameters is shown in Figure 6. The derived value of $N_{\rm H} \sim (1.2\text{–}1.3) \times 10^{21}$ $\rm cm^{-2}$ is comparable with (and even somewhat lower than) the galactic hydrogen column density in this direction ($N_{\rm H} \sim 1.5 \times 10^{21}$ $\rm cm^{-2}$; Dickey & Lockman 1990). No intrinsic absorption is required by the data, and no large variations are observed with radius. However, we note that, given the uncertainty in the background subtraction procedure described above, it is possible that we systematically underestimate the absorbing column density. The temperature shows a clear decrease from 7 keV at large radii to 3.7 keV near the center of the cluster, except for the very central region, which is contaminated by hard emission from the NGC 1275 nucleus. The abundance of heavy elements shows an opposite trend, decreasing (outside the central 1′–2′ region) with distance from the center.

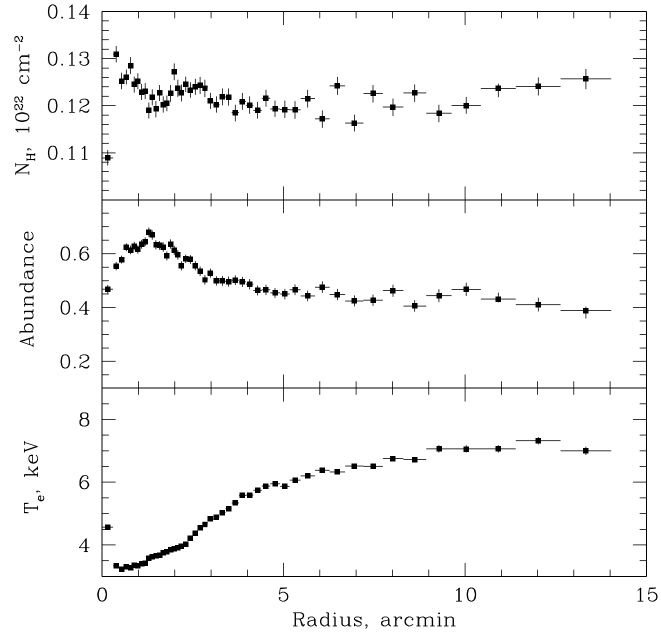

FIG. 6.—Radial profiles of $N_{\rm H}$, $T_e$, and heavy-element abundance calculated for a set of annuli centered at NGC 1275. The parameters were obtained using a single-temperature APEC model. The first two data points in the innermost region are affected by the presence of the bright compact source—the nucleus of NGC 1275.

### 3.3. *Asymmetric Surface Brightness Substructure*

As is clear from Figure 1 and known from earlier *Einstein* and *ROSAT* observations (Branduardi-Raymont et al. 1981), the surface brightness is not symmetric around NGC 1275. In order to further enhance the asymmetric structure, we plot in Figure 7 the relative deviations of the surface brightness from the azimuthally averaged surface brightness value (i.e., [data – model]/model). The resulting image has been smoothed with a 2″ Gaussian. Apart from the complicated structure in the innermost (∼2′) region probably dominated by the interaction of the thermal gas with the central AGN radio lobes (e.g., Böhringer et al., 1993; Churazov et al. 2000; Fabian et al. 2000, 2002) there are two regions of prominent excess emission on large scale—one ∼4′–7′ west of the center and one ≥5′ east of the center. The same structures were also clearly seen in earlier *ROSAT* PSPC and HRI images (e.g., Schwarz et al. 1992). The possible nature of these structures is further discussed in § 4.

### 3.4. *Deprojection Analysis*

The above radial dependencies of the gas parameters are affected by projection effects and the azimuthal asymmetry of the cluster. The first problem can be solved using deprojection analysis. Various flavors of deprojection techniques are frequently used (e.g., Fabian et al. 1981; Kriss, Cioffi, & Canizares 1983; McLaughlin 1999). In our analysis we assume spherical symmetry but make no specific assumption about the form of the underlying gravitational potential. We first calculate the surface brightness (in a given energy band) in a set of $n_a$ annuli and choose a set of $n_s$ spherical shells. The radii of the annuli and shells need not be the same. The gas parameters are assumed to be uniform inside each shell. The outermost radii of the annuli and shells are chosen so that $r(n_s) < r(n_a)$. The emissivity of the gas for radii larger than $r(n_s)$ is assumed to decline with the radius as a power law with a given slope, namely, $\mathcal{E} = \mathcal{E}_0 r^{-4}$. The normalization of this extra component $\mathcal{E}_0$ is an additional free parameter of the model. One can then

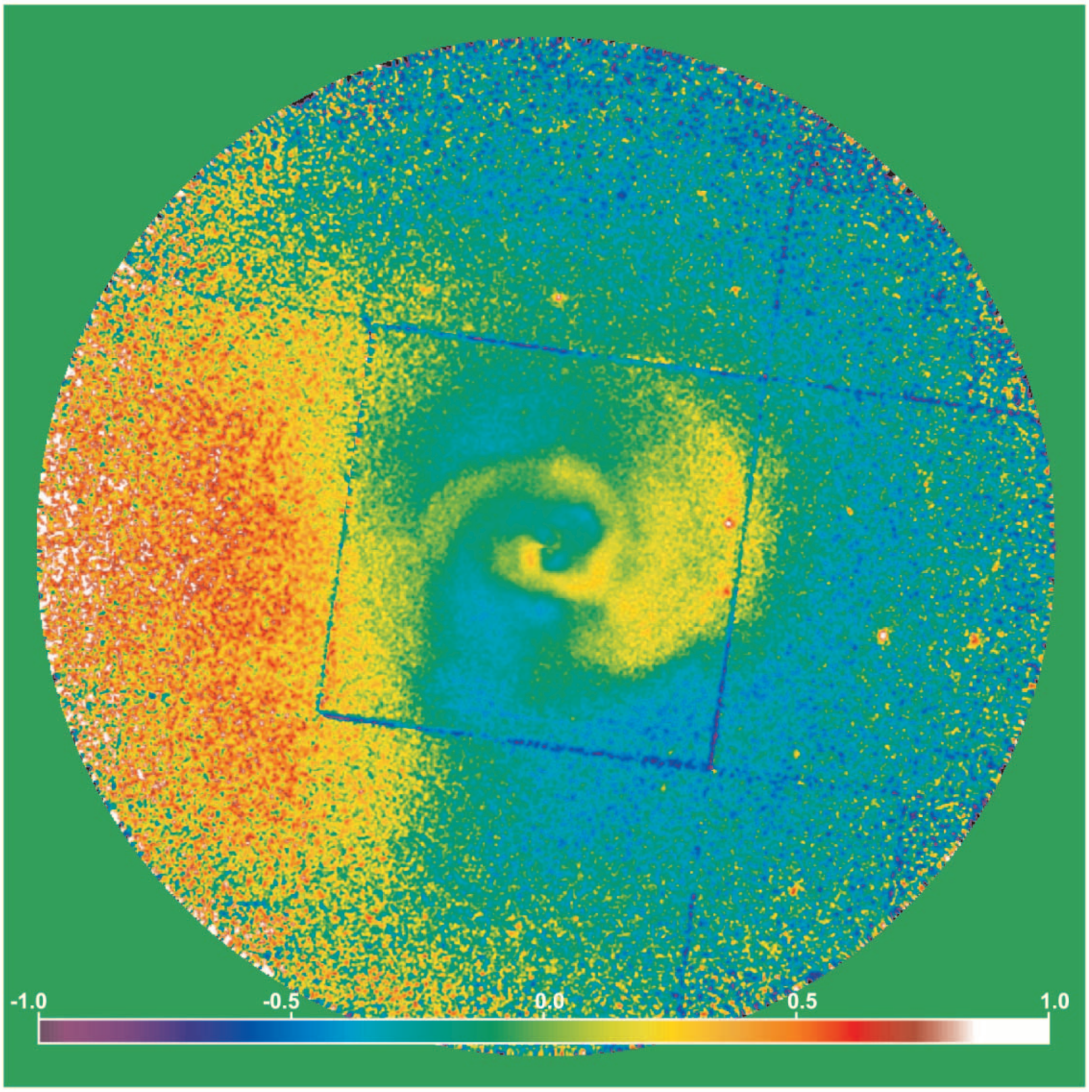

Fig. 7.—Relative deviation of the surface brightness from the azimuthally averaged value. The image shown is 30′ × 30′. Clearly seen are the region of excess emission to the east from the center, an edgelike structure 5′–7′ to the west from the center, and complicated structure in the inner 1′–2′ region.

write a simple expression that describes the contribution of all shells and outer regions from $r(n_s)$ to infinity to the surface brightness $S(j)$ in a given annulus $j$:

$$S(j) = \sum_{i=1,n_s} A(i,j)\mathscr{E}(i) + B(j)\mathscr{E}_0 \ , \qquad (1)$$

where $\mathscr{E}(i)$ is the emissivity of a given shell. A simple analytical expression for $A(i,j)$ and $B(j)$, which are functions of the radii of corresponding shell and annulus, can easily be written (e.g., Kriss et al. 1983; McLaughlin 1999).

We then formulate a least-squares problem to find which set of emissivities in our set of shells will provide the best description of the surface brightness recorded in our set of annuli:

$$\sum_j \left[ \sum_i A(i,j)\mathscr{E}(i) + B(j)\mathscr{E}_0 - S(j) \right]^2 \Big/ \sigma_j^2 = \min \ , \qquad (2)$$

where $\sigma_j$ is the statistical error associated with the surface brightness in a given annulus. As usual, the differentiation of this relation with respect to $S(j)$ and $\mathscr{E}_0$ yields a system of linear equations, which can easily be inverted. The properties of the inverse matrix $C(j,i)$ (in particular an error enhancement due to an ill-conditioned problem) can be easily controlled by making the spherical shells broader. The emissivities of the shells are then expressed through the observed surface brightness distribution as an explicit linear combination,

$$\mathscr{E}(i) = \sum_{j=1,n_a} C(j,i)S(j) \ . \qquad (3)$$

We then accumulate a set of spectra (corrected for the background and vignetting) for each annulus. The emission spectrum associated with each shell can then be calculated as the same linear combination of the observed spectra. Since the whole procedure is linear the (statistical) errors can be propagated straightforwardly. The resulting spectra for every shell are fitted with standard models in XSPEC. The radial dependence of the electron density, temperature, and heavy-element abundance is shown in Figure 8. As usual for any kind of deprojection analysis, the errors on the deprojected values of temperature and abundance are significantly larger than for the projected spectra. However, the biggest uncertainty in the deprojected parameters probably comes from the assumption of spherical symmetry. As is clear from § 3.3, the cluster is significantly asymmetric. Furthermore, when deriving the density in a given shell we assume that X-ray–emitting gas uniformly fills the volume of the shell. Nonetheless we present below two simple analytical approximations to the density and temperature distributions that crudely characterize the radial behavior of these two parameters (Fig. 8, *solid lines*):

$$n_e = \frac{3.9 \times 10^{-2}}{\left[1 + (r/80)^2\right]^{1.8}} + \frac{4.05 \times 10^{-3}}{\left[1 + (r/280)^2\right]^{0.87}} \ \mathrm{cm}^{-3} \ , \qquad (4)$$

where the second term is the density distribution on larger scales taken from Jones & Forman (1999) and is shown in Fig. 8 (*dotted line*),

$$T_e = 7\,\frac{\left[1 + (r/100)^3\right]}{\left[2.3 + (r/100)^3\right]} \ \mathrm{keV} \ . \qquad (5)$$

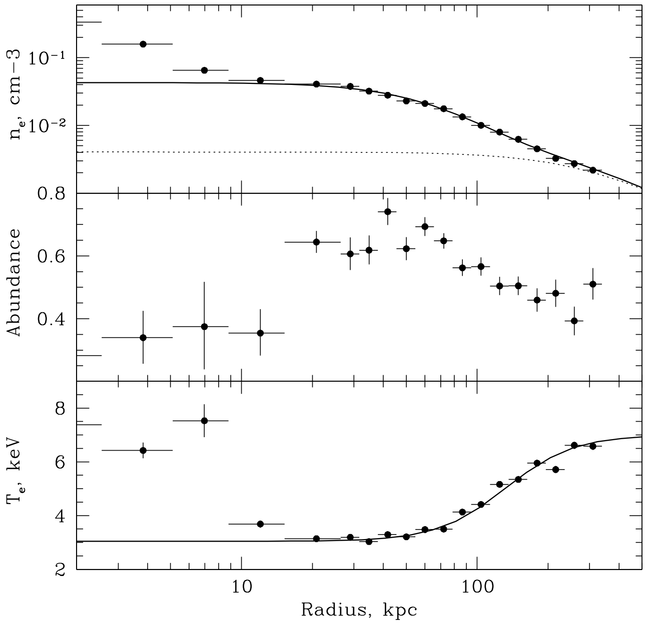

FIG. 8.—Radial profiles of deprojected parameters. The parameters were obtained using a single-temperature APEC model with fixed low-energy absorption fitted to deprojected spectra for a set of spherical shells centered at NGC 1275. The data points in the innermost region (~10 kpc) are affected by the presence of the bright compact source—the nucleus of NGC 1275. Analytical approximations for the density and temperature are shown as solid lines (see text).

The analytical approximations shown in Figure 8 clearly fail to follow the data in the innermost region (within the central ~10 kpc). Given the *XMM-Newton* angular resolution, the major problem here is the contribution from the bright compact source—the nucleus of NGC 1275. This makes *Chandra* much more suitable for studies of the innermost region.

Schmidt et al. (2002), using *Chandra* data and excluding the contribution from the nucleus, showed that within about 50 kpc, the deprojected temperature profile is essentially flat (see their Fig. 7), with a mean of approximately 3.1 keV, in excellent agreement with the *XMM-Newton* temperature values from 10–50 kpc (away from the region in which the nuclear source contributes to the *XMM-Newton* spectral data). The temperature profile derived from the projected *Chandra* spectra in finer radial bins (Schmidt et al. 2002, their Fig. 2) does, however, show a slight increase in temperature in the innermost (<10 kpc) bin. It is possible that projection effects (due to the presence of X-ray " holes " in the inner region) increase the apparent gas temperature there somewhat. Therefore, equation (5), with its essentially constant temperature at $r < 50$ kpc, is a reasonable approximation. A comparison of the azimuthly averaged *Chandra* surface brightness profile in the inner region with the *XMM-Newton* data also shows that a gas-density profile with a flat core (eq. [4]) is a reasonable approximation to the data.

### 3.5. *Projected Temperature Structure*

To calculate the projected gas temperature distribution, we employed the method described in Churazov et al. (1996, 1999) and applied previously to the *ASCA* data (e.g., Donnelly et al. 1998, 2001). Briefly, we use template spectra corresponding to emission from an optically thin plasma (convolved with the MOS energy response) temperatures of 3 and 9 keV with a given metallicity and low-energy photoelectric absorption to determine the best-fit weights of these template spectra needed to describe the spectrum $S(E)$ observed in a given pixel of the image, i.e.,

$$S(E) = A \times M(T_1, E) + B \times M(T_2, E) \ , \qquad (6)$$

where $M(T, E)$ is the template spectrum for a given value of temperature $T$. The temperature is then calculated as a function of the relative weights of the template spectra. As is shown in Churazov et al. (1996), an expectation value of the temperature calculated this way is usually very close (within a few percent) to the temperature obtained by conventional spectral fitting under the assumption of a single-temperature plasma with fixed metallicity and absorption. Compared to hardness ratios, typically used for the same purpose, this method is significantly more sensitive. The determination of weights is a linear procedure (i.e., fast), and further smoothing can be applied after the images containing weights are calculated. The resulting temperature map for Perseus is shown in Figure 9. An adaptive smoothing has been applied to the map in such a way that each value of the temperature has been calculated using regions containing $\sim 10^4$ counts. Comparison with the results of direct spectral fitting for individual regions shows good agreement with the overall temperature structure.

Compared with the previous *ASCA* temperature maps (Arnaud et al. 1994; Furusho et al. 2001), *XMM-Newton* data show the innermost region in much greater detail, while the global asymmetry is broadly consistent with the lower resolution *ASCA* maps, which cover a much larger area. The temperature structure of the very central region (within $1'$–$2'$) is consistent with the recent *Chandra* results (Fabian et al. 2000; Schmidt et al. 2002).

On the spatial scales of $1'$–$15'$, which are particularly well mapped by the *XMM-Newton* observations, the most remarkable feature of the temperature map is a horseshoe-shaped high-temperature region to the west that envelops the central cooler region. Thus the global east-west asymmetry of the cluster seen in the surface brightness distribution (Fig. 7) is also clearly present in the gas temperature distribution.

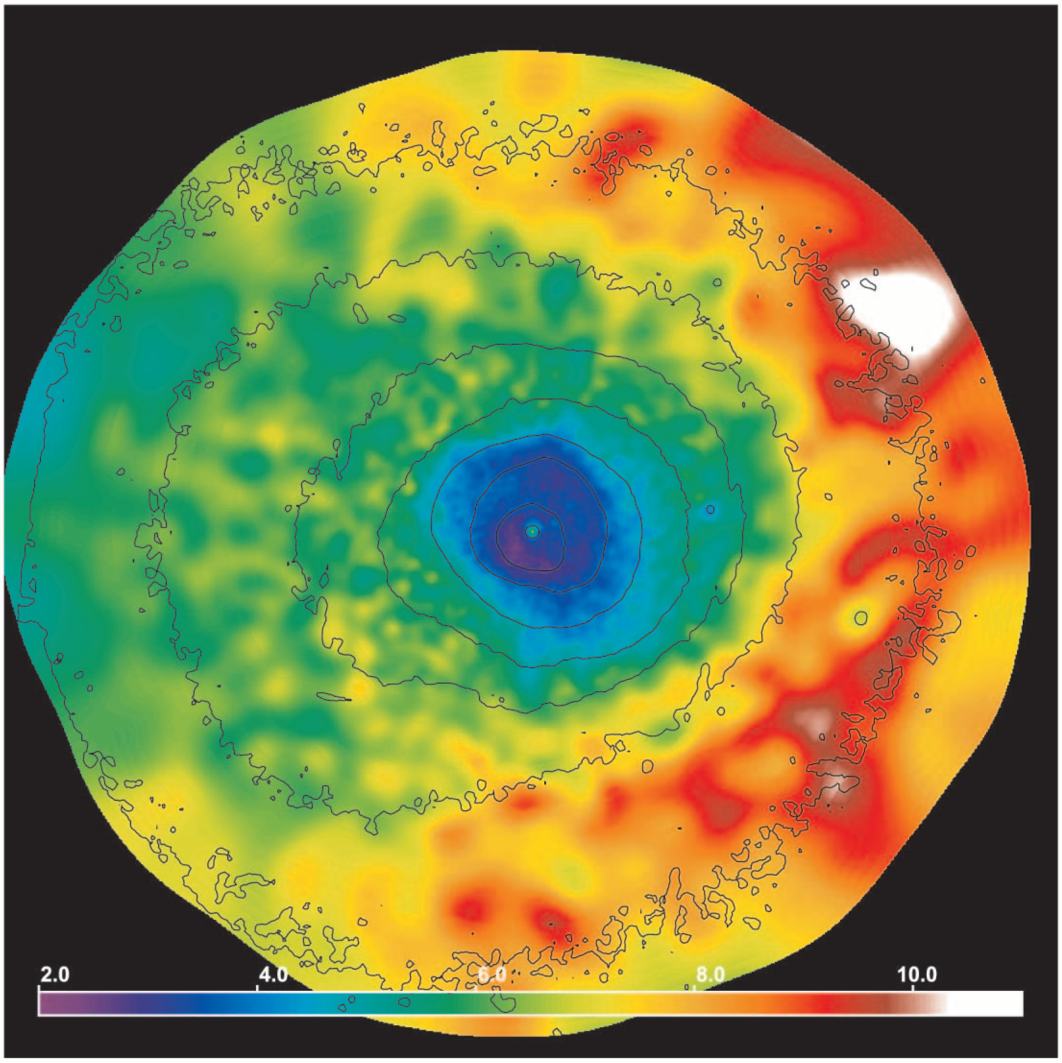

Fig. 9.—Gas temperature map ($30' \times 30'$). The temperature is derived from adaptively smoothed data with an effective number of counts within each smoothing window of $\sim 10^4$. Contours show the surface brightness distribution.

If the cluster gas is in a state of a hydrostatic equilibrium, then the gas density and temperature should remain constant along the equipotential surfaces set by the gravitating mass. In the example of a spherical or elliptical potential, all features in the observed surface brightness or temperature distribution should reflect the symmetry of the underlying potential. Shocks or strong sound waves (e.g., produced by a merger) may reveal themselves as distinct features in the observed images or temperature maps. The variations of density and temperature in shocks are obviously correlated, leading to a positive correlation of the variations in surface brightness images and temperature maps. The observed variations (Figs. 7 and 9), on the contrary, suggest that in Perseus the variations of the temperature and surface brightness are anticorrelated. One can see that all the most prominent positive features in Figure 7 correspond to regions of lower (relative to the mean value at the same distance from the center) temperature. To show this more clearly in Figure 10, we plot side by side the deviations of the surface brightness and temperature from the azimuthally averaged values. The surface brightness image $I$ and the temperature map $T$ can be further combined in the form of two additional images, $P = T\sqrt{I}$ and $S = T/I^{1/3}$. Since the surface brightness scales as the square of the electron density (i.e., $I \propto n_e^2$), then $P \propto Tn_e$ and $S \propto T/n_e^{2/3}$. Therefore these two images, $P$ and $S$, can be used to approximately characterize the azimuthal variations of pressure and entropy[5] in the gas. These variations are also shown in Figure 10. It is clear that the relative amplitude of the azimuthal variations in pressure is smaller than that for any of the other quantities shown in Figure 10, and there is no clear east-west asymmetry in the pressure distribution. This argues against attributing the bulk of the observed substructure in the surface brightness distribution and temperature to strong shocks. Instead, the observed features clearly resemble edges or "cold fronts" found recently in several clusters (e.g., Markevitch et al. 2000, 2002; Vikhlinin, Markevitch, & Murray 2001). The possible origin of this substructure is discussed below.

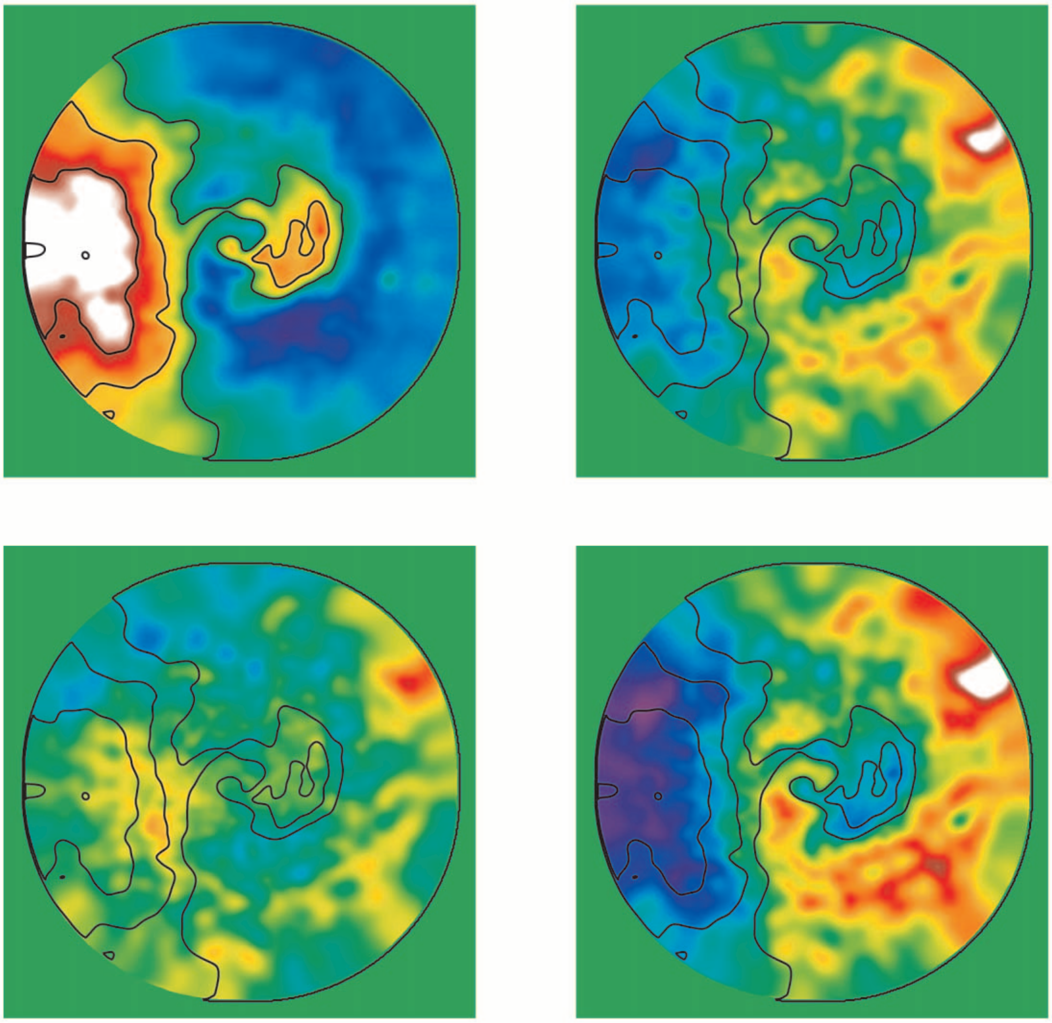

FIG. 10.—Relative deviations from azimuthly averaged values of (*a*) surface brightness $I$, (*b*) temperature $T$, (*c*) pressure $p = T\sqrt{I}$, and (*d*) entropy $s = T/I^{1/3}$. Contours mark the regions of excess surface brightness (from the first image). The color scale is the same for all three plots (from −0.5 to +0.5; see color bar in Fig. 7). Clearly the azimuthal variations in pressure are smaller than in any other quantity.

---

[5] We use the term entropy for the quantity $S = T/n_e^{2/3}$; the true specific entropy is determined by the logarithm of this quantity.

## 4. DISCUSSION

During its lifetime, any cluster experiences a few major mergers with another cluster of comparable mass and much more frequent accretion of smaller clusters or groups. A chain of bright optical galaxies extending to the west from NGC 1275 suggests that at present the Perseus Cluster is merging with a subcluster coming from that direction. The effect of a merger on the appearance of the cluster obviously depends strongly on the mass ratios and gas fractions of merging clusters (see recent reviews by Evrard & Gioia 2002; Sarazin 2002; Schindler 2002 and references therein). Given that the deviations from spherical symmetry in the surface brightness and temperature, although clearly present, are not very large, then we probably have a case of a merger with a relatively small subcluster or group of galaxies. Furthermore, the lack of large azimuthal pressure variations (Fig. 10) suggests that we are observing the merger in a late stage when strong shocks have already left the central region of the cluster mapped with *XMM-Newton*. The numerical (*N*-body and fluid dynamics) simulations of the merger most relevant for the Perseus case are probably those of Gomez et al. (2002). Their merger 7 (see Table 1 from Gomez et al. 2002) has a mass ratio of 1 : 16 and a small gas fraction for the subcluster so that the cooling flow is not disrupted during the merger. One can see some features in the gas density and temperature distributions in their simulations (Figs. 5 and 6 in Gomez et al., 2002) that are qualitatively similar to the structures found in the Perseus data.

In Perseus the most striking feature is a clear edge in the surface brightness, which separates cooler gas in the very core from the hotter horseshoe-shaped region in the west, enveloping the core. One plausible explanation of these structures is a contact discontinuity separating the main-cluster gas from the gas of the infalling subcluster. The shape of the contact discontinuity depends primarily on the density profiles of colliding clusters. For two identical clusters involved in a head-on merger, the contact discontinuity is a plane perpendicular to the line connecting the centers of two clusters and located half way between the centers. In the case of a merger of a rich cluster with a smaller and less dense subcluster, the contact discontinuity shifts toward the center of the smaller subcluster and bends as the result of the stronger impact of the ram pressure on the outer regions of the smaller subcluster, giving the infalling gas a conical shape (see, e.g., Fig. 5 in Gomez et al. 2002). The presence of a very dense core in the main cluster may reverse this trend and bend the contact discontinuity in the opposite direction so that it will envelop the very core of the main cluster. This behavior is less obvious in the simulations by Gomez et al. (2002), although flattening of the contact discontinuity is definitely seen. Assuming that merger 7 of Gomez et al. (2002) is a close analog of the Perseus merger, one would conclude that the present state of the Perseus Cluster corresponds to a time ~0.25 Gyr after the core crossing, when the contact discontinuity is located within ~200 kpc of the center of the main cluster (their Fig. 4, *upper right-hand panel*). After 0.5–0.75 Gyr the dense and cold gas of the main cluster rebounds and shifts the bulk of the subcluster gas to larger distances from the center (their Fig. 4, *middle right-hand panel*).

An alternative explanation of the edge and horseshoe structures in Perseus assumes that the contact discontinuity is located farther away from the cluster core and that the observed structures are composed solely from the disturbed gas of the main cluster. If the chain of bright galaxies marks the ongoing accretion direction of very small groups of galaxies, it is possible that (given the richness of Perseus) in each individual merger event the gas of the infalling subcluster is decelerated far from the Perseus core and never comes close to the center. Such a situation resembles the picture of a piston that initially is moving through the gas but then stops. The gas in the core of the Perseus Cluster would then see a compression wave (shock) followed by a rarefaction wave. The gas density and temperature increase during the compression phase but then decrease as the gas reexpands. There should be only a modest increase in the final gas temperature associated with the increase of the entropy in the shock. The velocity of the gas in the core of the main cluster also first increases and then falls back to zero, with the net effect that every volume element of gas is displaced some distance from its initial position. Since the density, temperature, and pressure change significantly across the core (particularly in the direction perpendicular to the direction of the compression wave motion), the impact of the passing compression/rarefaction wave will differ in terms of the increase in temperature and the net displacement. If the characteristic amplitude of the wave propagating through the nonuniform medium scales as the square root of the density $n_e$, then the amplitude of the initial displacement at a distance $r$ from the center $X(r)$ scales as $(1/[n_e(r)])^{1/2}$. Therefore the wave would induce a smaller net displacement in the very core region (where the density is the highest) than in the region farther from the core. Such a process can lead to characteristic " horseshoe " structures in the temperature and density distributions that are qualitatively similar to those observed in the Perseus Cluster. However, the relative amplitude of the displacement $X(r)/r \propto (1/[n_e(r)r^2])^{1/2}$ is a decreasing function of radius for density profiles less steep than $r^{-2}$. Therefore the relative amplitude of the displacement in the very core of the cluster will still be strong. The displaced gas in the core will then try to restore hydrostatic equilibrium and oscillate in the potential.

We illustrate the bending of the shock and the induced oscillatory motion of the gas in the core with a simple numerical simulation of a plane compression wave passing through a cluster gas. The simulations were made using the ZEUS-2D code (Stone & Norman 1992a, 1992b). In our simulations we employed an ideal gas equation of state with $\gamma = 5/3$. Equations (4) and (5) were used for the initial density and temperature distributions. The gravitational potential was calculated from the same density and temperature distributions and assumed to be static. The computational domain spans a $6 \times 4$ Mpc region and is covered by $600 \times 400$ grid points. At some distance from the cluster, we modify the gas velocity, density, and temperature in a slab 200 kpc wide to mimic the situation when a piston is first driven into a cluster gas with a Mach number of ~2 and then stops. The results shown below were obtained from the simulations on a Cartesian grid, while simulations on the cylindrical grid produce qualitatively very similar results.

Snapshots of the gas density distribution at several successive moments of time (0, 0.3, 0.7, and 1.6 Gyr from the beginning of the simulations) are shown in Figure 11. Initially the plane shock bends, when passing through the core, because of the higher pressure and lower temperature in the central region. Shortly after the passage of the wave through

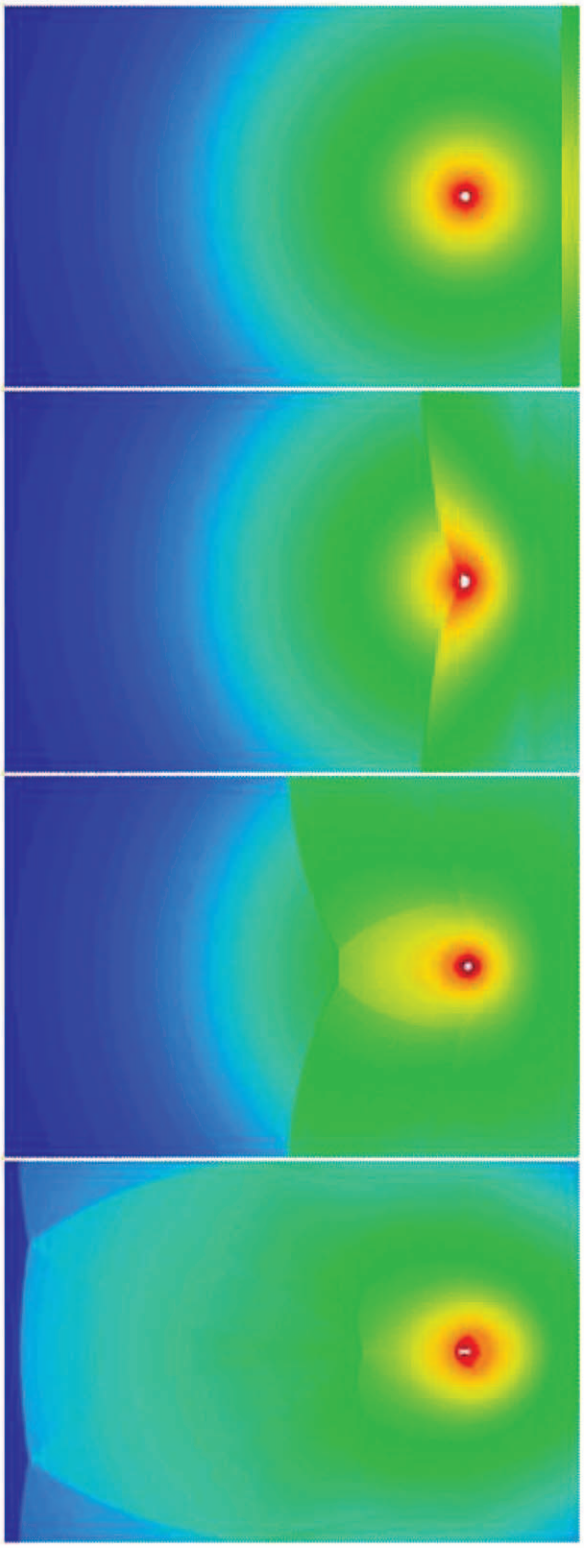

FIG. 11.—Snapshots of the gas density at 0, 0.3, 0.7, and 1.6 Gyr from the beginning of the simulations. The box shown is 4 × 6 Mpc. The density, temperature, and velocity of the gas in a narrow slab on the right-hand side of the box were set to mimic the impact of a piston that is first driven into the gas at the Mach number of 2 and then suddenly stopped.

the core, the gas distribution is clearly elongated in the direction of motion, with the very core regions experiencing smaller displacements than the outer layers. The gas then begins "sloshing" (this term was introduced in Markevitch, Vikhlinin, & Mazzotta 2001; see also Markevitch et al. 2002) in the potential well, which in our case is assumed to be static. To show the structure of the density distribution more clearly, we plot the relative deviation of the gas density from the undisturbed value in Figure 12. The first frame corresponds to the time when the shock front is passing through the core. Although originally the gas is swept in the direction of the wave propagation, in ~0.5 Gyr it rebounds and produces excess emission on the opposite side of the core. The relevant timescales for the gas sloshing are probably set by the acoustic cutoff frequency $w_a$ and the buoyancy (Brunt-Väisälä) frequency $N$, which can be written as

$$w_a = \frac{c_s}{2}\frac{d\ln P}{dr}\ , \tag{7}$$

$$N = \Omega_{\rm K}\sqrt{\frac{1}{\gamma}\frac{d\ln s}{d\ln r}}\ , \tag{8}$$

where $s$ is the gas entropy, $r$ is the radius, and $\Omega_{\rm K}$ is the Keplerian frequency at a given radius. The dependence of the acoustic cutoff and the buoyancy frequencies on radius (using the density and temperature profiles according to eqs. [4] and [5]) are shown in Figure 13.

While strictly speaking these frequencies are determined by the local properties of the gas (and we are interested in global oscillations), it is likely that they set an approximately correct timescale for the gas sloshing. Since these frequencies vary with radius, the gas will slosh with different periods, with the possibility of forming several asymmetric structures at the same time on either side of the core. This is illustrated in Figure 12, where the deviation of the gas density from the undisturbed value is shown at several times. The structures seen in the density distribution resemble the cold edges or fronts observed by *Chandra* in many clusters (e.g., Markevitch et al. 2002). The edges in this simulation are due to sloshing of the cluster core gas and are of course transient events, which, however, can persist for a few gigayears, although their shapes evolve continuously. As usual for oscillatory motion, the gas spends most of the time near one of the points of maximum displacement, i.e., in the configuration favorable for the detection of the disturbed gas as an "edge."

From Figure 13, the shortest period of sloshing is on the order of 1 Gyr. This means that it takes about a 0.5 Gyr for the gas displaced by the initial shock to rebound to the opposite side of the center of the potential and form an edge there. If this mechanism is responsible for the formation of the edge in the Perseus Cluster, then we can roughly estimate that the initial shock has passed through the core some 0.5 Gyr before. On such timescales the primary wave has enough time to propagate outside the region mapped with *XMM-Newton* and the disturbed dense gas in the center has enough time to rebound.

In this interpretation the increase of gas entropy on the western side of the cluster (see Fig. 10) can be attributed to the initial shock or sequence of shocks. If the gas in that region was originally on the same adiabat as now observed at the eastern side of the cluster then in a single-shock interpretation the increase of entropy by ~50% (estimated from Fig. 10) would require a shock with a Mach number of ~2.6. Assuming that the gravitating mass profile of the Perseus Cluster follows the Navarro-Frenk-White (1997) profile with the parameters obtained by Ettori, De Grandi,

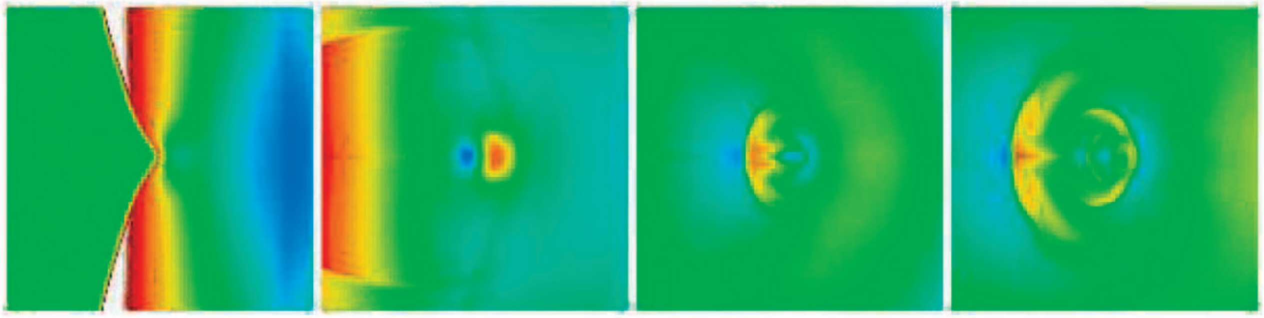

FIG. 12.—Relative deviation of the gas density from the initial value (the blue color marks the regions with the density below the initial value, while yellow and red correspond to overdense regions). The box shown is approximately 2 Mpc on a side. The snapshots are taken at 0.3, 0.7, 2.3, and 3.9 Gyr from the beginning of the simulation.

& Molendi (2002), we can estimate that the free-fall velocity reaches a Mach number of 2.6 (for 6.5 keV gas) at a distance of ~300 kpc from the cluster center. This is of course an upper limit on the velocity of the contact discontinuity, attainable only if the infalling gas is sufficiently dense. Depending on the geometry of the contact discontinuity, the forward shock will have a velocity similar to the velocity of the discontinuity (e.g., bow shock) or slightly higher (for a plane-parallel shock). Therefore the observed asymmetry in the entropy distribution is only marginally consistent with the assumption that a single shock was responsible for the entropy increase. Multiple small accretion events from roughly the same direction, which can be expected if there is indeed a large-scale filament in the direction set by the chain of bright galaxies, could more easily provide the observed rise of the entropy.

The motion of the cD galaxy relative to the larger scale potential of the cluster has long been suspected to play a role in clusters with cool and dense cores (e.g., David et al. 1994; Fabian et al. 2001; Markevitch et al. 2001). Since the distinction between the cD potential and cluster potential may be somewhat artificial, one can think instead in terms of perturbations of the potential in the cluster core. The gas can then start sloshing in the disturbed potential (e.g., Markevitch et al. 2001, 2002). We argue above that pure hydrodynamics may cause similar sloshing. What matters is the displacement of the gas relative to hydrostatic equilibrium, which can be achieved through disturbances in either the gas or the gravitating mass. In real mergers, both mechanisms are probably operating.

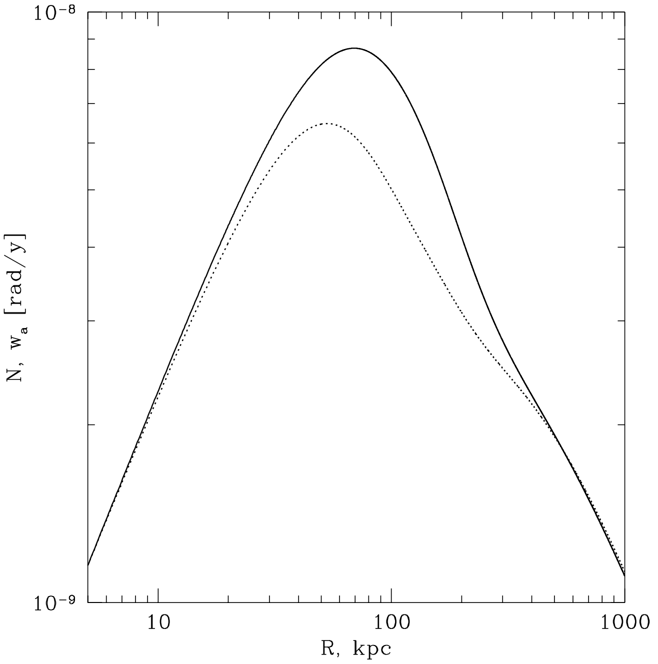

FIG. 13.—Buoyancy $N$ (*solid line*) and acoustic cutoff $w_a$ (*dotted line*) frequencies as a function of radius.

Markevitch et al. (2001, 2002) suggested that dissipation of the sloshing kinetic energy may be sufficient to offset radiative gas cooling. Assuming that the asymmetry in the surface brightness distribution in the inner 200 kpc region around NGC 1275 directly characterizes the amount of sloshing energy, one can estimate this energy as 10%–20% of the thermal energy of the gas. At a radius of 100 kpc, the cooling time is comparable to the sloshing turnaround time ($P = 2\pi/w_a$ or $P = 2\pi/N$), and at 200 kpc it is several times longer than the sloshing time. Assuming that this energy is dissipated over several sloshing turn around times (and neglecting the fact that part of the energy would be emitted as acoustic waves that escape the region), we conclude that the dissipated energy is not sufficient to offset cooling. However, the magnitudes (for cooling and dissipation) are comparable, and one can imagine scenarios in which the dissipation of the sloshing kinetic energy plays a more important role. In particular, our estimate that the sloshing energy constitutes 10%–20% of the thermal energy may be an underestimate.

### 4.1. *The Fate of the Stripped Gas*

During the merger process the subcluster gas is stripped from the dark matter potential of the infalling subcluster and mixes with the main cluster gas. As was pointed out by Fabian & Daines (1991), the infalling gas does not necessarily pass through a very strong shock during the merger process, and therefore the gas may remain on approximately the same adiabat as before the merger. This means that even stripped and decelerated lumps of subcluster gas may continue to move toward the center of the main cluster if their entropy is low enough. Even neglecting mixing with the main cluster gas, this motion can continue only until the lump reaches the radius in the main cluster where the main cluster gas has the same entropy as the lump. In Figure 14 we plot the entropy (defined as $T_e/n_e^{2/3}$) profile of the gas in the Perseus Cluster. One can compare the values of the

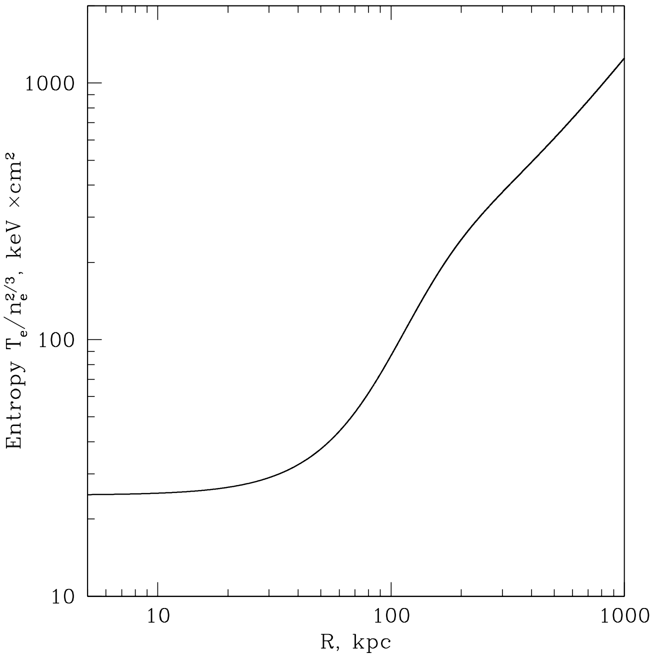

FIG. 14.—Radial gas entropy profile calculated as $T_e/n_e^{2/3}$ using the deprojected density and temperature profiles.

entropy with the characteristic values of the entropy found in clusters and groups (e.g., Ponman, Cannon, & Navarro 1999; Lloyd-Davies, Ponman, & Cannon 2000), which exceed ∼100 keV cm$^2$ even for poor groups. Thus, even if the infalling gas does not pass through a strong shock, which would further increase its entropy, it will find gas with comparable entropy at a distance at least several hundred kiloparsecs from the Perseus core. The infalling gas cannot easily penetrate below this radius. Therefore the core of the Perseus Cluster is well "protected" against penetration by infalling gas (unless the infalling subcluster itself contains a cool core with low-entropy gas).

### 4.2. *Mergers in the Absence of a Dense* (*Cool*) *Core*

The picture discussed above assumes that the main cluster contains a very dense (cool) core, while the infalling subcluster does not. In reality, various combinations of these parameters are possible, leading to a wealth of different appearances for mergers. In particular, if the main cluster lacks a dense (cool) core and the entropy of the infalling gas is significantly lower than that of the main cluster, the infalling gas may penetrate deep into the cluster core. The infalling cooler gas will be progressively stripped (Fabian & Daines 1991) from the dark matter halo and partly mixed with the main cluster gas. Even when stripped, the gas remains overdense compared to the main cluster gas and it will keep moving (although more slowly) toward the bottom of the potential well. This would result in a "cool wedge" penetrating deep inside (or even crossing) the main cluster. This kind of structure is probably observed in A1367 (W. Forman et al. 2003, in preparation) and in Coma. Both clusters have very high values for the gas entropy in their cores, so it is relatively easy for infalling gas to penetrate the core. Thus the cores in such clusters may appear much more disturbed than the cores of the "cooling flow" clusters, even if the infalling subclusters have similar parameters.

Thus if the main cluster does not have a dense and cool core, the gas from smaller infalling subclusters may penetrate deep into the cluster and mix with the main cluster gas. One can therefore expect the abundance of heavy elements to be more or less uniform throughout the cluster. However, when the main cluster has a dense cool core, the infalling gas is stopped before reaching the core and only small lumps from any cool cores in the infalling groups themselves are "allowed" to penetrate deeper. These *infalling* cool lumps are generally centered on a bright galaxy and are presumably also enriched in metals compared to the bulk of the subcluster gas, which is stopped at larger distances from the center of the main cluster. Therefore this process may serve to maintain (or even enhance) the radial abundance gradients observed in many clusters with cool cores.

## 5. CONCLUSIONS

We present the first results of the 50 ks *XMM-Newton* observations of the Perseus Cluster. The surface brightness and the gas temperature maps show a wealth of substructure on all spatial scales.

The inner region (1′–2′) is clearly disturbed by the interaction of the outflow of relativistic plasma from NGC 1275 with the thermal gas. On larger scales the horseshoe structure of the gas temperature and the surface brightness structure suggest an ongoing merger along the direction defined by a chain of bright (optical) galaxies. The gas from the infalling subcluster may be stripped from the dark matter halo at a large distance from the core of the Perseus Cluster, with only compression/rarefaction waves passing through the core of the main cluster. These waves may induce "sloshing" in the gas in the cluster core. As a result an "edge" (or even several edges) in the surface brightness and in the gas temperature distribution may appear.

Similar structures may be present in other clusters with peaked (cool) cores that are presently accreting smaller subclusters (e.g., Centaurus Cluster). For clusters without a cool dense core, the situation may be different since the subcluster gas is cool and can penetrate deep inside the core of the main cluster and form a cool wedge of partially stripped and mixed gas (e.g., Coma, A1367).

We thank Jean Ballet, Michael Freyberg, Marat Gilfanov, Sebastian Heinz, Nail Inogamov, Francesco Miniati, Ewald Müller, and Rashid Sunyaev for valuable discussions. W. F. and C. J. thank MPA for its hospitality during their summer 2002 visits and acknowledge support from the Smithsonian Institution and NASA (NAS 8-39073 and NAG 5-9944). We acknowledge use of the Digitized Sky Survey prepared by ST ScI (NASA grant NAG W-2166) from photographic data obtained with support from the National Geographic Society to California Institute of Technology. This work is based on observations obtained with *XMM-Newton*, an ESA science mission with instruments and contributions directly funded by ESA Member States and the US (NASA).

## REFERENCES

Anders, E., & Grevesse, N. 1989, Geochim. Cosmochim. Acta, 53, 197

Arnaud K. A. 1996, in ASP Conf. Ser. 101, Astronomical Data Analysis Software and Systems V, ed. G. Jacoby & J. Barnes (San Francisco: ASP), 17

Arnaud, K., et al. 1994, ApJ, 436, L67

Böhringer, H., Voges, W., Fabian, A. C., Edge, A. C., & Neumann, D. M. 1993, MNRAS, 264, L25

Branduardi-Raymont, G., Fabricant, D., Feigelson, E., Gorenstein, P., Grindlay, J., Soltan, A., & Zamorani, G. 1981, ApJ, 248, 55

Churazov, E., Forman, W., Jones, C., & Böhringer, H. 2000, A&A, 356, 788

Churazov, E., Gilfanov, M., Forman, W., & Jones, C. 1996, ApJ, 471, 673

———. 1999, ApJ, 520, 105

Conselice, C. J., Gallagher, J. S., & Wyse, R. F. G. 2001, AJ, 122, 2281

David, L., Jones, C., Forman, W., & Daines, S. 1994, ApJ, 428, 544

Dickey, J., & Lockman, F. 1990, ARA&A, 28, 215

Donnelly, H., Forman, W., Jones, C., Quintana, H., Ramirez, A., Churazov, E., & Gilfanov, M. 2001, ApJ, 562, 254

Donnelly, H., Markevitch, M., Forman, W., Jones, C., David, L., Churazov, E., & Gilfanov, M. 1998, ApJ, 500, 138

Ettori, S., De Grandi, S., & Molendi, S. 2002, A&A, 391, 841

Ettori, S., Fabian, A., & White, D. 1998, MNRAS, 300, 837

Evrard, A. E., & Gioia, I. M. 2002, in Merging Processes in Galaxy Clusters, ed. L. Feretti, I. M. Gioia, & G. Giovannini (Dordrecht: Kluwer), 253

Fabian, A. C., Celotti, A., Blundell, K. M., Kassim, N. E., & Perley, R. A. 2002, MNRAS, 331, 369

Fabian, A., & Daines, S. 1991, MNRAS, 252, P17

Fabian, A., Hy, E., Cowie, L., & Grindlay, J. 1981, ApJ, 248, 47

Fabian, A. C., Sanders, J. S., Ettori, S., Taylor, G. B., Allen, S. W., Crawford, C. S., Iwasawa, K., & Johnstone, R. M. 2001, MNRAS, 321, L33

Fabian, A., Zarnecki, J., Culhane, L., & Hawkins, F. 1974, ApJ, 189, L59

Fabian, A., et al. 2000, MNRAS, 318, L65

Forman, W., Kellogg, E., Gursky, H., Tananbaum, H., & Giacconi, R. 1972, ApJ, 178, 309

Furusho, T., Yamasaki, N. Y., Ohashi, T., Shibata, R., & Ezawa, H. 2001, ApJ, 561, L165

Gómez, P. L., Loken, C., Roettiger, K., & Burns, J. O. 2002, ApJ, 569, 122

Gorenstein, P., Fabricant, D., Topka, K., Harnden, F. R., Jr., & Tucker, W. H. 1978, ApJ, 224, 718

Jones, C., & Forman, W. 1999, ApJ, 511, 65

Kriss, G., Cioffi, D., & Canizares, C. 1983, ApJ, 272, 439

Lloyd-Davies, E., Ponman, T., & Cannon, D. 2000, MNRAS, 315, 689

Lumb, D., Warwick, R., Page, M., & De Luca, A. 2002, A&A, 389, 93

Malina, R., Bowyer, C., Lea, S., & Lampton 1978, ApJ, 219, 795

Markevitch, M., Vikhlinin, A., & Forman, W. 2002, preprint (astro-ph/0208208)

Markevitch, M., Vikhlinin, A., & Mazzotta, P. 2001, ApJ, 562, L153

Markevitch, M., et al. 2000, ApJ, 541, 542

McLaughlin, D. E. 1999, AJ, 117, 2398

McNamara, B., O'Connell, R., & Sarazin, C. 1996, AJ, 112, 91

Minkowski, R. 1957, IAU Symp. 4, Radio Astronomy, ed. H. C. van der Hulst (Cambridge: Cambridge Univ. Press), 107

Navarro, J. F., Frenk, C. S., & White, S. D. M. 1997, ApJ, 490, 493

Pedlar, A., Ghataure, H., Davies, R., Harrison, B., Perley, R., Crane, P., & Unger, S. 1990, MNRAS, 246, 477

Ponman, T., Cannon, D., & Navarro, J. 1999, Nature, 397, 135

Sarazin, C. 2002, in Merging Processes in Galaxy Clusters, ed. L. Feretti, I. M. Gioia, & G. Giovannini (Dordrecht: Kluwer), 1

Schindler, S. 2002, in Merging Processes in Galaxy Clusters, ed. L. Feretti, I. M. Gioia, & G. Giovannini (Dordrecht: Kluwer), 229

Schmidt, R., Fabian, A., & Sanders, J. 2002, MNRAS, 337, 71

Schwarz, R., Edge, A., Voges, W., Böhringer, H., Ebeling, H., & Briel, U. 1992, A&A, 256, L11

Sijbring, D. 1993, Ph.D. thesis, Groningen Univ.

Smith, R. K., Brickhouse, N. S., Liedahl, D. A., & Raymond, J. C. 2001, ApJ, 556, L91

Stone, J., & Norman, M. 1992a, ApJS, 80, 753

———. 1992b, ApJS, 80, 791

Strauss, M. A., Huchra, J. P., Davis, M., Yahil, A., Fisher, K. B., & Tonry, J. 1992, ApJS, 83, 29

Vikhlinin, A., Markevitch, M., & Murray, S. S. 2001, ApJ, 551, 160

Wolff, R., Helava, H., Kifane, T., & Weisskopf, M. 1974, ApJ, 193, L53